An Ultrathin Monolithic *XY* Nanopositioning Stage Constructed From a Single Sheet of Piezoelectric Material

Andrew J. Fleming 🆔 , *Member, IEEE*, and Yuen Kuan Yong 🆔 , *Member, IEEE*

Abstract—The paper describes an *XY* nanopositioning stage constructed from flexures and actuators machined into a single sheet of piezoelectric material. Ultrasonic machining is used to remove piezoelectric material and create electrode features. The constructed device is 0.508 mm thick, and has a travel range of 8.6 μm in the *X* and *Y* axes. The first resonance mode occurs at 597 Hz, which makes the device suitable for a wide range of standard nanopositioning applications where cost and size are considerations. Experimental atomic force microscopy is performed using the proposed device as a sample scanner.

Index Terms—Atomic force microscopy, nanopositioning, piezoelectric actuators.

I. INTRODUCTION

NANOMETER resolution positioning systems are used extensively in applications where a sample, probe, or substrate is scanned or statically positioned [1]. Scanning applications include atomic force microscopy [2]–[7] and data storage [8] while nonscanning applications include nanofabrication [9], [10], cell surgery [11], and precision optics [12]. Nanopositioning systems typically use piezoelectric actuators and a feedback system to eliminate actuator nonlinearity and reject external disturbances [13]–[15].

The first common nanopositioning systems were based on the piezoelectric tube scanner, which was famously used to demonstrate the scanning tunneling microscope in 1986 [16]. These monolithic tube structures are economical and can provide subatomic resolution. However, to achieve a useful scan-range, for example, $50 \times 50 \times 10$ μm ($X \times Y \times Z$), they must be physically long (50 mm) and therefore suffer from low-resonance frequencies and significant cross-coupling between the lateral and vertical axes [17]–[19].

To improve the speed and reduce out-of-axis motion, flexure-based nanopositioners were developed. These devices use piezoelectric actuators to drive a moving platform guided by metal flexures [20]–[24]. The high flexural stiffness dramatically reduces cross-coupling and allows a much larger payload than monolithic devices. However, flexure-based nanopositioners are considerably more costly, heavier, and bulkier than monolithic devices.

This paper describes a new class of nanopositioning system that is monolithic in structure but also incorporates flexural motion guidance. Previous monolithic nanopositioners were primarily extruded; however, the proposed device is constructed by removing material from a piezoelectric sheet by ultrasonic machining. By adding surface electrodes, active flexures are formed that generate displacement and guide the resulting motion. The stiffness, resonance frequencies, and travel range can be varied by changing the geometry of the flexures and electrode coverage. Furthermore, multiple different devices can be constructed on the same sheet of material, for example, multiple two-axis scanners with differing travel ranges and resonance frequencies.

In this work, a 0.508 mm thick sheet is used to create an *XY* nanopositioning stage that can translate an 18×18 mm load by up to 10 μm. This device is an order of magnitude thinner than the nearest comparable nanopositioner design. The small size allows a new range of applications in optomechanics, atomic force microscopy, and particularly, scanning electron microscopy where the load-lock area may be less than 5 mm in height [25]. The low cost is also a significant advantage which may enable the cost of scanning probe microscopes to be significantly reduced.

A. Contributions

A preliminary version of this work was presented at the IEEE conference on Advanced Intelligent Mechatronics in 2016 [26]. In this work, the electrode features were created using a Nitric acid printing process; however, this paper describes an ultrasonic milling process for both bulk material removal and surface electrode patterning. This was found to be superior. Other major revisions since the conference article include the following.

1) Revision of the boundary conditions to match the experimental bonded condition. This provides much closer agreement between finite-element analysis (FEA) and experimental results.
2) The voltage range is reduced to -200 to $+500$ V to match the safe operating range of the material.
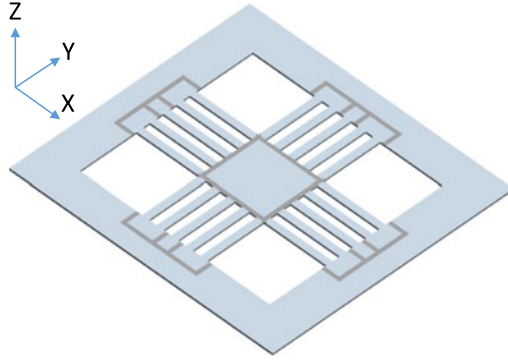
Fig. 1.   Proposed monolithic *XY* nanopositioning stage where the silver color represents nickel electrode and gray represents piezoelectric material.

3) Time-domain and frequency-domain characterization is performed in all three axes, including cross-coupling.
4) Atomic force microscopy is demonstrated in Section VII.
5) The maximum payload, cross-coupling, and robustness are analyzed in Section VIII.

In the following section, the overall design is described, followed by an in-depth analysis of the vertical stiffness and resonance frequency in Section III. Finite element simulations are presented in Section IV followed by a description of the fabrication process in Section V. Experimental results and a demonstration of atomic force microscopy are presented in Sections VI and VII. Practical considerations and conclusions are then discussed in Sections VIII and IX.

II. DESIGN

As illustrated in Fig. 1, the proposed design consists of a thin piezoelectric sheet with a number of cuts designed to create parallel beams that drive a central platform. The entire bottom surface is covered by a single grounded electrode. A simplified diagram of the structure and top electrode is shown in Fig. 2. Assuming that the poling vector is in the $+Z$-direction, a positive voltage applied to the top surface will cause the beam to expand and displace the central platform away from the positive voltage. For example, when a positive voltage is applied to the $+Vx$ electrode, the central platform will translate in the $+X$-direction. To develop the greatest deflection and force, the $+Vx$ and $-Vx$ electrodes are driven in a push–pull configuration as described in Fig. 2.

To model the motion of the platform, a single beam of length L_f is first considered. Assuming that the bottom surface is grounded and that the poling vector is in the $+Z$-axis, the free elongation ΔL can be derived from the standard piezoelectric equations [27]

$$\Delta L = L_f d_{31} E = \frac{L_f d_{31}}{t} V \tag{1}$$

where d_{31} is the piezoelectric strain constant, L_f is the length, E is the electric field, t is the thickness, and V is the applied voltage.

Although piezoelectric actuators are typically modeled as displacement actuators as described above, this simplification is
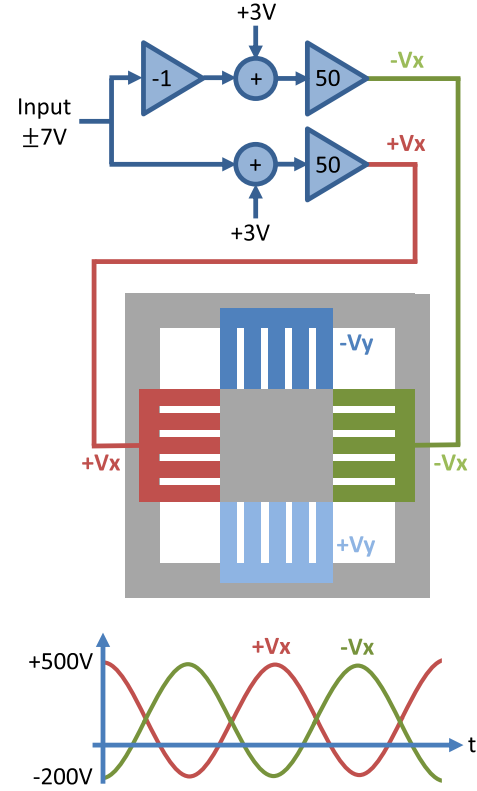

Fig. 2.   Scheme for generating the *X*-axis push–pull voltages. The gain of 50 is the high-voltage amplifier.

only valid when there is no load force or interconnected structure. For structures with interconnected actuators, the use of force and stiffness is more appropriate. By beginning with the stress-charge form of the piezoelectric constituent equations [27], the generated force and associated stiffness can be derived

$$F_a = d_{31} k_a V, \quad k_a = \frac{c^E A}{L_f} \tag{2}$$

where c^E is Young's modulus of elasticity, A is the cross-sectional area, and k_a is the internal stiffness derived by considering the axial mechanics of a bar. This model structure allows multiple parallel actuators to be modeled by a summation of the forces and stiffness.

If the electrodes on opposite sides are driven asymmetrically in a push–pull configuration, the total force is doubled. Therefore, with N beams on either side, the total force and stiffness are

$$F_a^* = 2N d_{31} k_a^* V, \quad k_a^* = 2N \frac{c^E A}{L_f}. \tag{3}$$

The total deflection can be derived from $\Delta L = F_a^* / k_a^*$, which reduces to $\Delta L = L_f d_{31}/t\, V$, which is identical to the free extension of a single beam.

In this work, the flexure length is chosen to be L_f=17 mm with a thickness of $t = 0.5$ mm. Therefore, the predicted deflection is

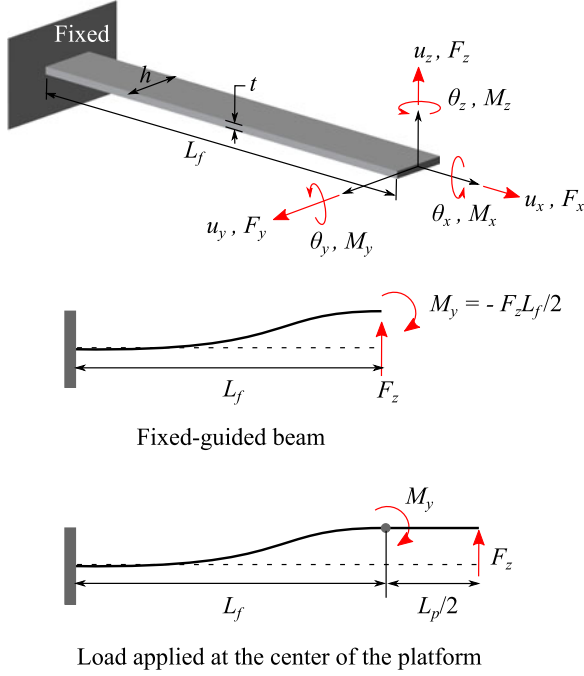$$\Delta L = \frac{L_f d_{31}}{t} V = V \times 6.5 \text{ nm/V}. \tag{4}$$

Fig. 3. Schematic of a beam-like flexure with loadings.

Since the maximum applied voltage is 700 V peak-to-peak, the predicted displacement range is 4.6 μm peak-to-peak. If the maximum positive voltage is extended to $+1000$ V, the predicted displacement is increased to 7.8 μm peak-to-peak.

III. MODELING

In this section, the effective stiffness, mass, and resonance frequency in the vertical (Z) direction are derived. Due to the planar design of the proposed device, the vertical resonance modes dominate the frequency response. Therefore, it is of particular interest to understand the first resonance mode and be able to predict how it is affected by factors such as geometry, external forces, and additional mass.

A. Effective Stiffness in the Z-Axis

The strain energy method and Castigliano's second theorem [28] are used to derive the effective stiffness of each flexure. Castigliano's second theorem is a simple and intuitive technique that allows the calculation of elastic bodies' deformation under external and reaction loadings acting at that location [28], [29]. This method has been widely used in designing flexure-guided nanopositioners [24], [30]. Using Castigliano's second theorem, the vertical displacement u_z of the beam flexure in Fig. 3 is defined as [24], [28], [30]

$$u_z = \left(\frac{L_f^3}{3EI_y} \right) F_z + \left(\frac{L_f^2}{2EI_y} \right) M_y \quad (5)$$

where L_f is the length of the flexure, E is the Young's modulus, and $I_y = ht^3/12$. Under the boundary condition of a fixed-guided beam, the resultant moment at the guided end of the beam due to the applied load F_z at that point is $M = -F_z L_f/2$.

Note that F_z is actually applied at the center of the platform as shown in Fig. 3. Therefore, the resultant moment M_y at the guided end of the beam is

$$M_y = F_z \frac{L_p}{2} - F_z \frac{L_f}{2}$$
$$= \frac{F_z}{2} (L_p - L_f) \quad (6)$$

where L_p is the length of the platform. Substituting (6) into (5) yields

$$u_z = F_z \left[\frac{L_f^3}{3EI_y} + \frac{L_f^2 (L_p - L_f)}{4EI_y} \right]. \quad (7)$$

Hence, the stiffness of the flexure in the Z-direction is

$$k_z = \frac{F_z}{u_z} = \left[\frac{L_f^3}{3EI_y} + \frac{L_f^2 (L_p - L_f)}{4EI_y} \right]^{-1}. \quad (8)$$

Since all flexures are arranged in parallel, the total stiffness of the monolithic nanopositioner is

$$K_z = Nk_z \quad (9)$$

where N is the number of flexures.

B. Effective Mass and Resonance Frequency

The effective mass of the flexure m_{eff} is calculated using Rayleigh's principle [31]

$$m_{\text{eff}} = \rho A \int_0^l \left[\frac{z(x)}{z_{\max}} \right]^2 dx \quad (10)$$

where ρ is the material density, $A = ht$ is the cross-sectional area of the flexure, $z(x)$ is the shape function (vibration amplitude) of the flexure, and $z_{\max}$ is the maximum displacement of the flexure along the Z-direction. The shape function for a fixed-guided beam with F_z applied at its guided-end is

$$z(x) = -\frac{F_z}{12EI_y} (L_f - x)^2 (L_f + 2x). \quad (11)$$

The maximum displacement is $z_{\max} = -F_z L_f^3/(12EI_y)$. Thus,

$$\frac{z(x)}{z_{\max}} = \frac{(L_f - x)^2 (L_f + 2x)}{L_f^3}. \quad (12)$$

Substituting (12) into (10) and solving the integration give

$$m_{\text{eff}} = \frac{13}{35} \rho A L_f = \frac{13}{35} m_f \quad (13)$$

where m_f is the mass of each flexure. Knowing the mass of the platform $m_p = \rho L_p^2 t$, the effective mass of the nanopositioner can then be obtained by

$$M_e = N m_{\text{eff}} + m_p. \quad (14)$$

The resonance frequency in the Z-direction can be derived as

$$f_{\text{res}} = \frac{1}{2\pi} \sqrt{\frac{K_z}{M_e}}. \quad (15)$$

TABLE I
NANOPOSITIONER PARAMETERS

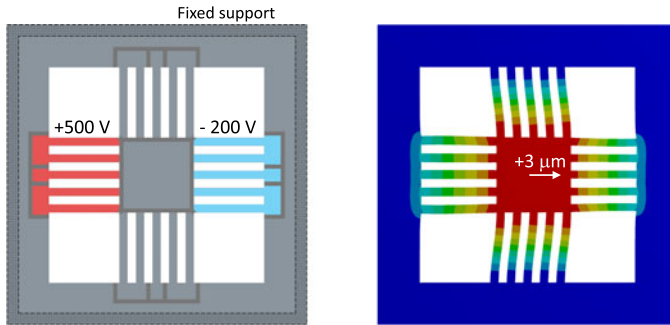| Description	Parameter	Value
Flexure length, mm	L_f	17
Flexure width, mm	h	2
Flexure thickness, mm	t	0.5
Platform length, mm	L_p	18
Number of flexures	N	20
Young's modulus, GPa	E	66
Density, kg/m^3	ρ	7800

Fig. 4. Finite-element simulation of the +X-axis full-scale deflection (right), resulting from the applied voltage (left). The shaded area represents a 2 mm bonded boundary condition.

TABLE II
PIEZOELECTRIC PROPERTIES FOR PZT-5A FROM PIEZO SYSTEM INC

Piezoelectric coefficient, C/m^2	
e_{31}	-10.92
e_{33}	12.08
e_{15}	12.29
Relative permittivity, $\varepsilon = \varepsilon^S/\varepsilon_\circ$	
ε_{11}	916
ε_{33}	830
Piezoelectric constant, pm/V	
d_{31}	-190

Substituting all the corresponding parameter values from Table I into (9), (14), and (15), the resonance frequency is $f_{res} = 425.6$ Hz.

IV. SIMULATION

An FE model of the piezoelectric nanopositioner was generated using ANSYS Workbench. Boundary conditions of the model are shown in Fig. 4 where the displacement of all four edges is fixed. Meshing was generated initially using the automesh tool. It was then refined manually to obtain more accurate results. The piezoelectricity of the nanopositioner is modeled using the ANSYS Coupled Field Physics Application Customization Toolkit extension. Table II lists the piezoelectric coefficients in stress form (e) and the relative permittivity $\varepsilon^S/\varepsilon_\circ$ required for constructing the piezoelectric body in ANSYS. The polarization vector of the piezoelectric material is in the +Z-direction. The maximum displacement of the X-axis was
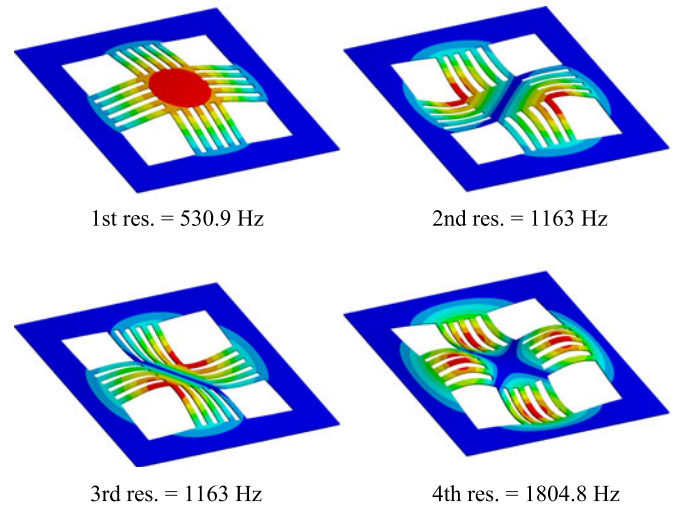

1st res. = 530.9 Hz   2nd res. = 1163 Hz

3rd res. = 1163 Hz   4th res. = 1804.8 Hz

Fig. 5. Finite element simulated resonance frequencies of the monolithic nanopositioner.

simulated by applying +500 and −200 V as shown in Fig. 4. The simulated displacement was ±3 μm in both lateral axes.

The resonance modes were simulated using the modal analysis module of ANSYS Workbench. The first four resonance modes are illustrated in Fig. 5. The vertical resonance mode appears at 530.9 Hz which is in close agreement with the analytical result, i.e., 425.6 Hz.

V. FABRICATION

The nanopositioner was fabricated from a monolithic sheet of PZT-5A with sputter-coated 5 μm Nickel electrodes. The sheet measures 72.3 × 72.3 × 0.508 mm and was obtained from Piezo Systems Inc. (T120-A4E-602). A number of methods for direct machining were attempted such as laser cutting, mechanical milling, and ultrasonic machining. Ultrasonic machining was the slowest method but provided excellent cut quality with no thermal damage to the material or electrodes. The working tool was a sintered diamond core drill, vibrating at 21 kHz and rotating at 8000 r/min. The cutting depth was 0.1 mm per pass. Using these machining parameters, precise lines could be milled through the PZT without causing significant heating or inducing the formation of fractures. The final shape and critical dimensions are illustrated in Fig. 6.

The electrodes were created with a single-pass cutting depth of 25 μm. Photolithography and direct acid printing were also trialed [26] but direct machining was found to produce sufficiently fine features without the need for chemical etching.

VI. EXPERIMENTAL RESULTS

The experimental setup consists of the nanopositioner mounted on a base as pictured in Fig. 7. For safety reasons, the device is mounted upside-down so that the top electrode is grounded and the high-voltage electrodes are inaccessible. The motion in each axis is measured simultaneously with a Polytec MSA-3D interferometer. A comparison of the analytical, finite element, and experimental performance is listed in Table III.
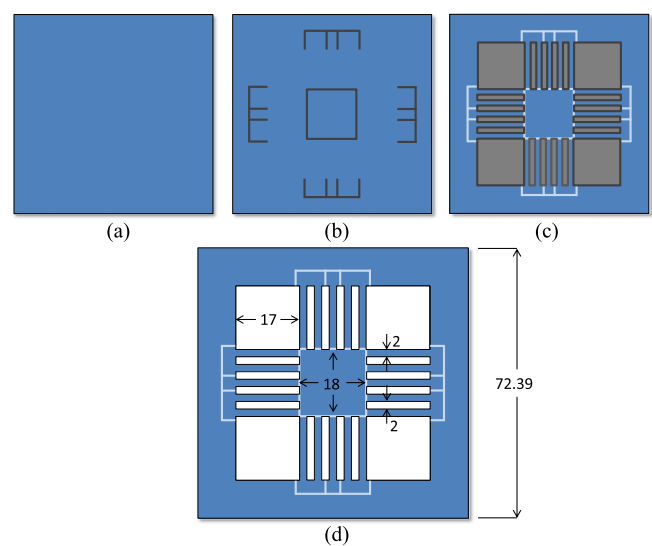
Fig. 6. (a) Fabrication sequence starting with a piezo sheet. (b) The surface electrodes are formed by subtractive surface machining, followed by (c) bulk machining, and resulting in the (d) finished device.
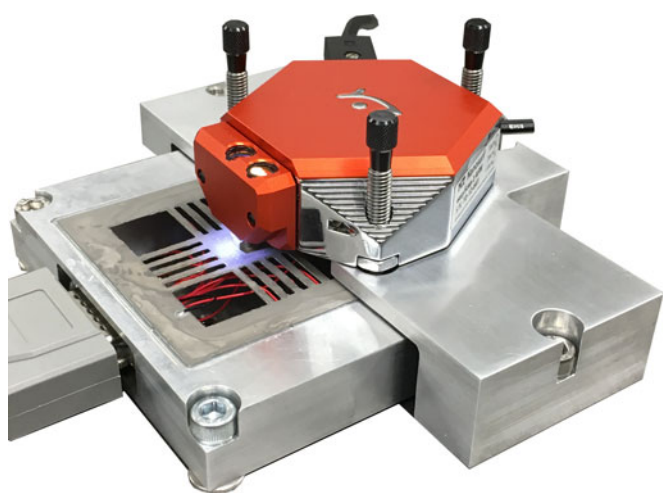

Fig. 7. Monolithic stage mounted underneath a Nanosurf AFM head.

TABLE III
COMPARISON OF THE ANALYTICAL, FEA, AND EXPERIMENTAL RESULTS

	Analytical	FEA	Experimental
X Travel (700 Vp-p)	4.6 μm	6.0 μm	8.6 μm
First Resonance Freq	426 Hz	531 Hz	597 Hz
Maximum Payload	21 g	19 g	N/A

To evaluate the travel range, both sides were driven asymmetrically with a 1 Hz sinusoidal voltage from -200 to $+500$ V. Note that $+500$ V is only half the positive voltage range but was chosen for safety reasons. The resulting lateral deflection is plotted in Fig. 8 which shows a travel range of 8.6 μm in X and 10.8 μm in Y. The X- and Y-axis travel range were both slightly higher than the predicted range, which was 4.6 μm analytically and 6.0 μm by FEA. The difference between the predicted and experimental range is presumed due to uncertainty in d_{31}
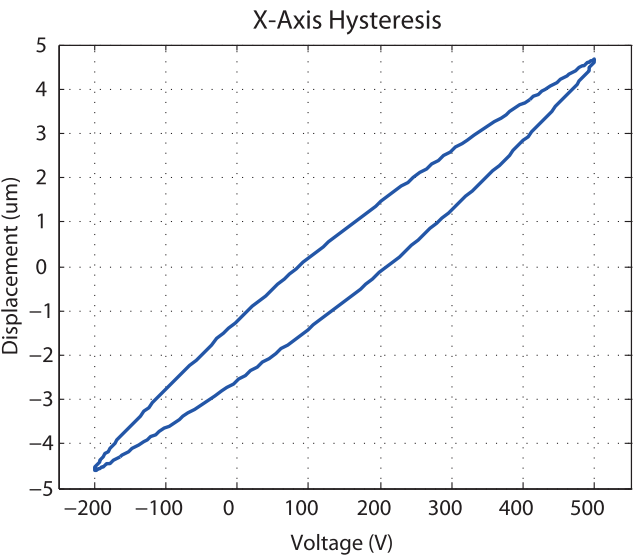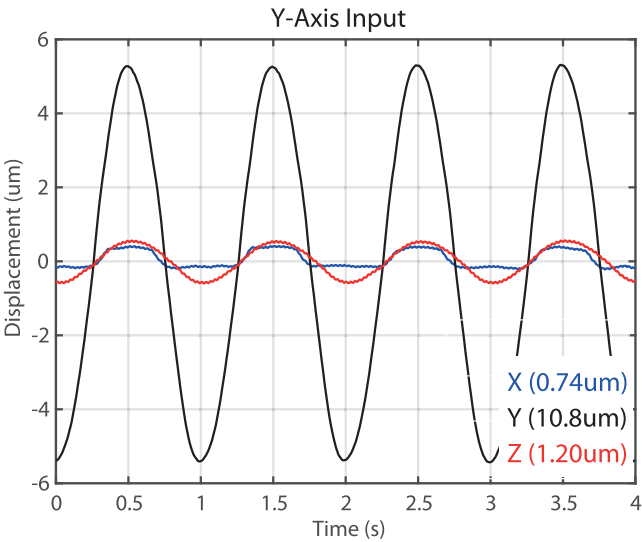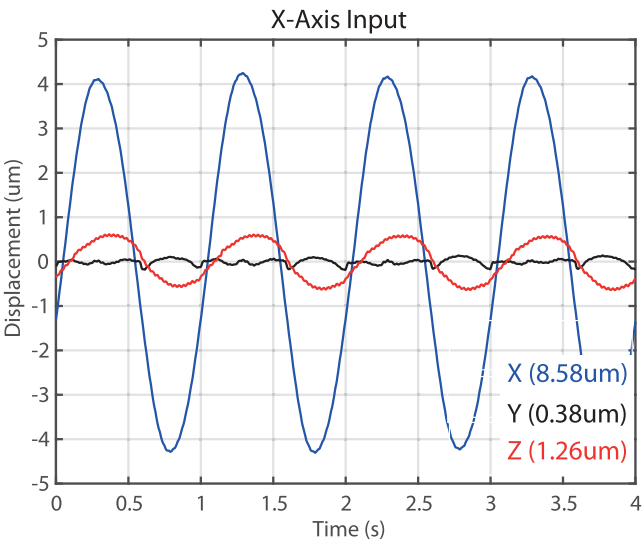

Fig. 8. X-, Y-, and Z-axis motion in response to a full-range 1 Hz sine wave applied to the X- and Y-axis (-200 to $+500$ V). The hysteresis in the X-axis is also plotted.
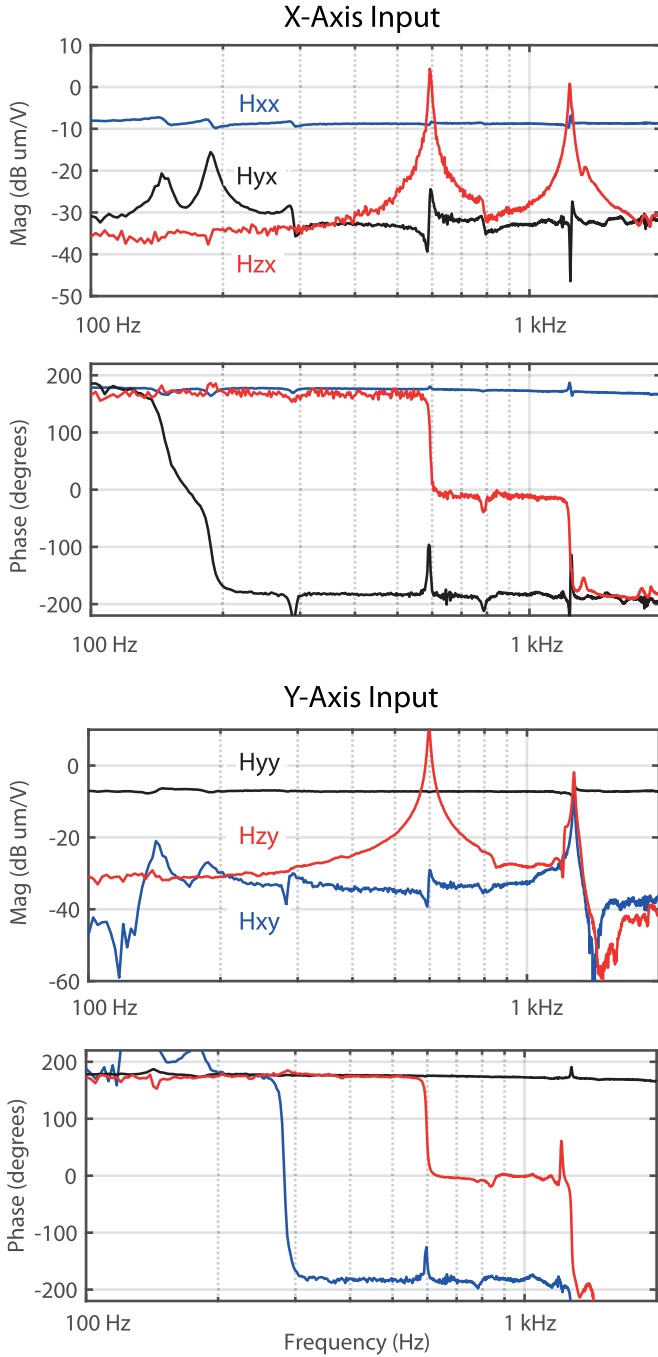
X-Axis Input

Y-Axis Input

Fig. 9. Measured frequency responses from the applied voltage to the X-, Y-, and Z-axis deflection (in μm/V). Hyx refers to the frequency response from the X-axis input to the Y-axis deflection, and so on.

and the magnitude of the applied voltage. Piezoelectric constants are quoted for small-signals; however, the nonlinearity of piezoelectric material results in significant differences when the full voltage range is utilized. The change in sensitivity versus voltage can be observed in the hysteresis plot in Fig. 8, which is typical of PZT-5A material.

In Fig. 9, the X- and Y-axis frequency responses exhibit a relatively constant response over a wide frequency range. However, the maximum useful frequency is limited by the first vertical mode measured at 597 Hz. This value compares well with the
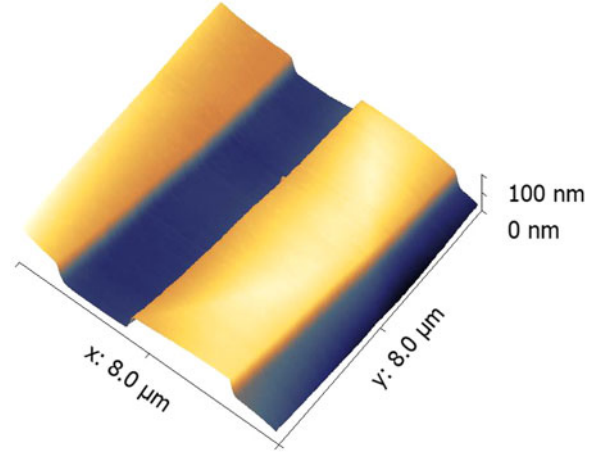

Fig. 10. Constant-force contact-mode AFM image of a calibration grating with a 5 μm period and 100 nm height.

finite element simulation (531 Hz) and the analytical prediction (426 Hz). The discrepancy is due to the 2 mm glue strip on the experimental system which slightly stiffens the structure. The small, low-frequency peaks are thought to be the resonance modes of the wires between the electrodes and connector. These wires have a significant mass relative to the structure, so their resonance modes can be seen in the response. In future, the electrical wiring will be integrated into the outside support structure of the device, which will eliminate wiring and the associated resonances.

VII. ATOMIC FORCE MICROSCOPE IMAGING

To demonstrate the application of the proposed nanopositioner, the experimental setup in Fig. 7 was used to obtain an 8×8 μm image of a Budget Sensors HG-100MG calibration grating. The grating is a rectangular array with a 5 μm period and 100 nm height. A contact-mode ContAl-G cantilever with a resonance frequency of 13 kHz was used to probe the sample. The grating was imaged in constant-force contact-mode using a Nanosurf EasyScan2 atomic force microscope (AFM) mounted on top of the nanopositioner. The contact force was regulated at 30 nN.

The calibration grating was placed on the central platform of the nanopositioner. To move the grating in a raster pattern, the X-axis of the nanopositioner was driven with a 0.5 Hz triangular waveform, and the Y-axis was driven with a ramp signal. The vertical signal of the AFM head was recorded and used to construct the image in Fig. 10. The image processing included the removal of a plane from image, which results from tilting of the sample and cross-coupling between the lateral and vertical axis. The effect of hysteresis can be observed in the image as the feature edges are not perfectly straight.

VIII. DISCUSSION

In Fig. 10, the monolithic stage is suitable for high-resolution AFM imaging despite the relatively high cross-coupling between the lateral axes (-20 dB or 10%), and between the lateral

and vertical axes (-25 dB or 6%). By comparison, a typical commercial nanopositioner would have a cross-coupling better than -30 dB (3%). Although the lateral cross-coupling is significant, this is not evident in the image since the artifact is image rotation. The vertical cross-coupling adds a sloping plane to the image, which is automatically removed in standard AFM image processing. For other applications such as lithography, the cross-coupling would need significant improvement. Current research involves the use of a three-axis closed-loop control and improvements to the mechanical design which reduce the lateral stiffness and increase the vertical stiffness.

The maximum payload is determined by the stress σ_f in the piezoelectric flexures, which was derived in [32]

$$\sigma_f = \frac{0.15 F_z L_f}{h t^2} \tag{16}$$

where σ_f is the stress, F_z is the vertical force, L_f is the flexure length, h is the flexure width, and t is the thickness. The maximum tensile strength of PZT-5A is 11 MPa [33]; therefore, the maximum vertical force is 2.1 N. To maximize the service life, it is desirable to avoid exceeding 10% of the maximum tensile stress, which corresponds to a vertical force is 0.21 N and a maximum payload mass of 21 g. Using finite element analysis, the maximum force and payload were found to be of 1.9 N and 19 g, respectively.

Typical metal-flexure nanopositioners have a maximum payload on the order of 500 g, which is 25 times greater than the proposed design; however, they are also typically 25 times thicker. The maximum 2.1 N vertical force of the monolithic stage means that it is less robust than a standard nanopositioner; however, this may be an acceptable trade-off given the simplicity, low-cost, and small dimensions.

Present research includes laminating multiple piezo-layers together to improve the vertical stiffness, robustness, and maximum payload; however, it is accepted that this detracts from the simplicity of the single-layer structure.

IX. CONCLUSION

This paper proposes a new method for designing and fabricating nanopositioning systems from a single sheet of piezoelectric material. Ultrasonic milling was used to construct a two-axis nanopositioner from active flexures and electrodes. Analytical and finite element models were derived which closely match the experimental response. A full-scale range of 8.6 μm was achieved with a resonance frequency of 597 Hz.

The completed nanopositioner is only 508 μm in thickness which is an order-of-magnitude thinner and lighter than the state-of-the-art. The proposed fabrication method has the potential to dramatically reduce the size and cost of many other positioning systems including rotational stages, vertical positioners, and mirror scanners.

Current work is focused on the integration of closed-loop sensors and the development of more complex geometries to improve the travel range and provide additional degrees of freedom such as rotation and vertical motion.

REFERENCES

[1] A. J. Fleming and K. K. Leang, *Design, Modeling and Control of Nanopositioning Systems*. London, U.K.: Springer, 2014.

[2] M. S. Rana, H. R. Pota, and I. R. Petersen, "Performance of sinusoidal scanning with MPC in AFM imaging," *IEEE/ASME Trans. Mechatronics*, vol. 20, no. 1, pp. 73–83, Feb. 2015.

[3] A. Bazaei, Y. K. Yong, and R. Moheimani, "Combining spiral scanning and internal model control for sequential AFM imaging at video rate," *IEEE/ASME Trans. Mechatronics*, vol. 22, no. 1, pp. 371–380, Feb. 2017.

[4] S. M. Salapaka and M. V. Salapaka, "Scanning probe microscopy," *IEEE Control Syst.*, vol. 28, no. 2, pp. 65–83, Apr. 2008.

[5] D. Y. Abramovitch, S. B. Andersson, L. Y. Pao, and G. Schitter, "A tutorial on the mechanisms, dynamics, and control of atomic force microscopes," in *Proc. Amer. Control Conf.*, New York, NY, Jul. 2007, pp. 3488–3502.

[6] A. J. Fleming, B. J. Kenton, and K. K. Leang, "Bridging the gap between conventional and video-speed scanning probe microscopes," *Ultramicroscopy*, vol. 110, no. 9, pp. 1205–1214, Aug. 2010.

[7] M. Fairbairn, S. O. R. Moheimani, and A. J. Fleming, "Q control of an atomic force microscope micro-cantilever: A sensorless approach," *J. Microelectromech. Syst.*, vol. 20, no. 6, pp. 1372–1381, Dec. 2011.

[8] A. Sebastian, A. Pantazi, H. Pozidis, and E. Eleftheriou, "Nanopositioning for probe-based data storage," *IEEE Control Syst.*, vol. 28, no. 4, pp. 26–35, Aug. 2008.

[9] S. Mishra, J. Coaplen, and M. Tomizuka, "Precision positioning of wafer scanners. Segmented iterative learning control for nonrepetitive disturbances," *IEEE Control Syst.*, vol. 27, no. 4, pp. 20–25, Aug. 2007.

[10] A. Ferreira and C. Mavroidis, "Virtual reality and haptics for nanorobotics," *IEEE Robot. Autom. Mag.*, vol. 13, no. 3, pp. 78–92, Sep. 2006.

[11] Z.-Q. Fan *et al.*, "Piezo-assisted in vitro fertilization of mouse oocytes with spermatozoa retrieved from epididymides stored at 4 degree C," *J. Reproduction Develop.*, vol. 54, no. 2, pp. 107–112, 2008.

[12] S. Z. S. Hassen, M. Heurs, E. H. Huntington, I. R. Petersen, and M. R. James, "Frequency locking of an optical cavity using linearquadratic gaussian integral control," *J. Phys. B, Atomic, Mol. Opt. Phys.*, vol. 42, no. 17, 2009, Art. no. 175501.

[13] S. K. Das, H. R. Pota, and I. R. Petersen, "Damping controller design for nanopositioners: A mixed passivity, negative-imaginary, and small-gain approach," *IEEE/ASME Trans. Mechatronics*, vol. 20, no. 1, pp. 416–426, Feb. 2015.

[14] S. Devasia, E. Eleftheriou, and S. O. R. Moheimani, "A survey of control issues in nanopositioning," *IEEE Trans. Control Syst. Technol.*, vol. 15, no. 5, pp. 802–823, Sep. 2007.

[15] A. J. Fleming, "Measuring and predicting resolution in nanopositioning systems," *Mechatronics*, vol. 24, no. 6, pp. 605–618, Sep. 2014.

[16] G. Binnig and D. P. E. Smith, "Single-tube three-dimensional scanner for scanning tunneling microscopy," *Rev. Sci. Instrum.*, vol. 57, no. 8, pp. 1688–1689, Aug. 1986.

[17] J. Maess, A. J. Fleming, and F. Allgöwer, "Simulation of dynamics-coupling in piezoelectric tube scanners by reduced order finite element models," *Rev. Sci. Instrum.*, vol. 79, Jan. 2008, Art. no. 015105.

[18] M. Ratnam, B. Bhikkaji, A. J. Fleming, and S. O. R. Moheimani, "PPF control of a piezoelectric tube scanner," in *Proc. IEEE Conf. Decis. Control Eur. Control Conf.*, Seville, Spain, Dec. 2005, pp. 1168–1173.

[19] Y. R. Teo, Y. K. Yong, and A. J. Fleming, "A comparison of scanning methods and the vertical control implications for scanning probe microscopy," *Asian J. Control*, vol. 19, no. 2, pp. 1–15, 2017. [Online]. Available: http://www.precisionmechatronicslab.com/wp-content/uploads/2017/01/J17d.pdf

[20] H. Tang and Y. Li, "A new flexure-based yθ nanomanipulator with nanometer-scale resolution and millimeter-scale workspace," *IEEE/ASME Trans. Mechatronics*, vol. 20, no. 3, pp. 1320–1330, Jun. 2015.

[21] K. W. Chae, W.-B. Kim, and Y. H. Jeong, "A transparent polymeric flexure-hinge nanopositioner, actuated by a piezoelectric stack actuator," *Nanotechnology*, vol. 22, no. 33, 2011, Art. no. 335501.

[22] L. L. Howell, *Compliant Mechanisms*. Hoboken, NJ, USA: Wiley, 2000.

[23] B. J. Kenton, A. J. Fleming, and K. K. Leang, "A compact ultra-fast vertical nanopositioner for improving SPM scan speed," *Rev. Sci. Instrum.*, vol. 82, no. 12, 2011, Art. no. 123703.

[24] Y. K. Yong, S. O. R. Moheimani, B. J. Kenton, and K. K. Leang, "Invited review article: High-speed flexure-guided nanopositioning: Mechanical design and control issues," *Rev. Sci. Instrum.*, vol. 83, no. 12, 2012, Art. no. 121101.

[25] C. Zhou *et al.*, "A closed-loop controlled nanomanipulation system for probing nanostructures inside scanning electron microscopes," *IEEE/ASME Trans. Mechatronics*, vol. 21, no. 3, pp. 1233–1241, Jun. 2016.

[26] A. J. Fleming, G. Berriman, and Y. K. Yong, "Design, modeling, and characterization of an XY nanopositioning stage constructed from a single sheet of piezoelectric material," in *Proc. 2016 IEEE Int. Conf. Adv. Intell. Mechatronics*, Banff, 2016, pp. 1333–1338.

[27] *IEEE Standard on Piezoelectricity*, ANSI/IEEE Std. 176–1987, 1988.

[28] N. Lobontiu, *Compliant Mechanisms: Design of Flexure Hinges*. Boca Raton, FL, USA: CRC Press, 2003.

[29] N. Lobontiu, J. S. N. Paine, E. Garcia, and M. Goldfarb, "Corner-filleted flexure hinges," *Trans. ASME, J. Mech. Des.*, vol. 123, pp. 346–352, 2001.

[30] B. J. Kenton and K. Leang, "Design, characterization, and control of a monolithic three-axis high-bandwidth nanopositioning stage," in *Proc. Amer. Control Conf.*, Baltimore, MD, 2010, pp. 4949–4956.

[31] W. Thomson, *Theory of Vibration With Applications*, 3rd ed. Englewood Cliffs, NJ, USA: Prentice-Hall, 1988.

[32] Y. K. Yong, "Preloading piezoelectric stack actuator in high-speed nanopositioning systems," *Front. Mech. Eng.*, vol. 2, 2016, Art. no. 8.

[33] D. Berlincourt, H. H. A. Krueger, and C. Near, "Properties of morgan electro ceramic ceramics," Morgan Electro Ceram., Cleveland, OH, USA, Tech. Publication 226, 2003.

Andrew J. Fleming (M'02) received the B.Sc. degree in electrical engineering and the Ph.D. degree in mechatronics engineering from the University of Newcastle, Callaghan, NSW, Australia, in 2000 and 2004, respectively.

He is currently an Australian Research Council Future Fellow and the Director with the Precision Mechatronics Lab, University of Newcastle. He is the co-author of three books, and more than 180 journal and conference articles. He is the Inventor of several patent applications. His research interests include lithography, nanopositioning, scanning probe microscopy, and biomedical devices.

Dr. Fleming received the Academy for Technological Sciences and Engineering Baterham Medal in 2016, the Newcastle Innovation Rising Star Award for Excellence in Industrial Engagement in 2012, the IEEE Control Systems Society Outstanding Paper Award in 2007, and the University of Newcastle Researcher of the Year Award in 2007.

Yuen Kuan Yong (M'09) received the B.S.E.E. degree in mechatronics engineering and the Ph.D. degree in mechanical engineering from the University of Adelaide, Adelaide, SA, Australia, in 2001 and 2007, respectively.

She is currently an Australian Research Council Discovery Early Career Researcher Award Fellow with the School of Electrical Engineering and Computing, University of Newcastle, Callaghan, NSW, Australia. Her research interests include nanopositioning systems, microcantilevers, high-speed atomic force microscopy, and miniature robotics.

Dr. Yong received the University of Newcastle Vice-Chancellor's Awards for Research Excellence and the Pro Vice-Chancellors Award for Excellence in Research Performance in 2014. She is an Associate Editor for the IEEE/ASME TRANSACTIONS OF MECHATRONICS and *Frontiers in Mechanical Engineering*.